Dispersive Optical Wireless Indoor Channels—From Frequency-Domain Modeling to Bit-Error-Rate Prediction

Henrik Schulze, *Member, IEEE*, Jan Mietzner, *Senior Member, IEEE*, and Peter Adam Hoeher, *Fellow, IEEE*

***Abstract*—Methods for calculating the impulse response of dispersive optical wireless channels have been known for a long time. However, a comprehensive procedure for predicting resulting bit error rates, starting from a highly accurate channel emulation method, has not yet been presented. To fill this gap, we propose a methodology for modeling realistic dispersive optical wireless channels that can be used directly for corresponding bit error rate simulations. The importance of proper power normalization of the multipath components is emphasized. Moreover, the optical channel model is embedded in an end-to-end electrical channel model suitable for intensity-modulation/direct detection schemes under linear operation. To significantly reduce the simulation time, a so-called chip-rate model is presented. Finally, based on the proposed modeling approach for dispersive channels, bit error rate simulations are performed for selected intensity modulation schemes with and without equalization at the receiver and are compared within a common and consistent framework.**

***Index Terms*—Bit error rate, channel models, equalizers, intensity modulation, multipath channels, optical wireless communication, visible light communication.**

I. Introduction

In TIMES of ever-increasing demands for high bandwidths in wireless communication applications, indoor visible-light communication (VLC) is an attractive option for complementing or – in certain sensitive environments even replacing – existing radio-transmission solutions, such as wireless local area networks [1]. If fully networked, VLC systems are referred to as light fidelity (Li-Fi) [2] and offer some unique advantages over radio-based solutions, such as reusability of existing lighting infrastructure, high energy efficiency, enhanced physical-layer security, potentially high data rates in an unregulated spectrum, and excellent electro-magnetic compatibility. Moreover, power-efficient digital modulation schemes allow for reliable data transmission even in the case of adaptive dimming [3], which is a common feature in state-of-art lighting systems.

Manuscript received 20 October 2023; revised 28 December 2023; accepted 17 January 2024. Date of publication 23 January 2024; date of current version 9 February 2024. *(Corresponding author: Henrik Schulze.)*

Henrik Schulze is with the South Westphalia University of Applied Sciences, D-59872 Meschede, Germany (e-mail: schulze.henrik@fh-swf.de).

Jan Mietzner is with the Faculty of Design, Media, and Information, Hamburg University of Applied Sciences, D-22081 Hamburg, Germany (e-mail: jan.mietzner@haw-hamburg.de).

Peter Adam Hoeher is with the Faculty of Engineering, Kiel University, D-24143 Kiel, Germany (e-mail: ph@tf.uni-kiel.de).

Digital Object Identifier 10.1109/JPHOT.2024.3357169

In indoor VLC settings, reflections are caused by walls and furnishings. Multipath propagation leads to dispersive channels, which can impair the digital transmission of data. On the other hand, reflected signal components may be vital for link maintenance in the case of line-of-sight (LOS) blockage. To investigate these effects on the bit error rate (BER) through simulations, it is necessary to describe these channels as realistically as possible. A first step in this direction was made in [3] by establishing an approach for joint light planning and error-rate prediction regarding dual-use VLC systems. However, only the received optical power has been considered in the approach taken in [3], whereas the dispersive structure of the channel was not taken into account. Further works on optical channel modeling for VLC applications were reported in [4], [5], [6], [7], [8], [9], [10], [11], but BER results deduced from these models were not reported therein.On the other hand, BER results for a particular intensity-modulation scheme were presented in [12], [13], but in [12] focus was not laid on detailed modeling of the optical channel, while in [13] a detailed analysis of the intersymbol interference (ISI) caused by the dispersive optical channel was omitted.

While methods for calculating the dispersive structure of optical wireless communication (OWC) channels via an impulse response have been known for a long time [14], none of the above references combines detailed geometrically-based channel emulations (for concrete room setups) with corresponding BER simulations in a consistent and unified framework. Either geometrically-based channel emulation is addressed and resulting channel properties (such as the root-mean-square delay spread or the coherence bandwidth) are investigated, or BER analyses are provided employing rather generic channel models (without direct reference to concrete geometrical settings). An interesting alternative to the time domain (TD) OWC channel modeling approach in [14] is the frequency domain (FD) method more recently proposed in [8], [11]. The benefit of the FD method is that it allows to sum up the infinite series of (diffuse) reflections of any order, which significantly improves the accuracy [11]. Yet, to the best of the authors's knowledge, a consistent methodology from efficient emulation of dispersive OWC channels to BER simulations is still missing.

The present work aims to fill this gap. We show how to use impulse responses obtained by the inverse Fourier transform from frequency responses calculated by the FD method described in [8], [11] to simulate bit error rates for realistic

optical indoor channels and practically relevant optical modulation schemes. Comparative numerical evaluations regarding the received optical power within a reference room showed a very good agreement between the FD method and the light simulation approach taken in [3], for which a high accuracy was attested in [15] (the interested reader is referred to the discussion in Section IV-F of [3]).

The present paper uses realistic FD simulations of optical wireless indoor channel as described in [8] and [11]. The latter work is a refinement of the first in the sense that a better accuracy can be reached at the same computational effort.

The frequency responses calculated from this method can be transformed to the time domain to obtain impulse responses that are suitable for BER simulations of optical modulation schemes like e.g. on-off keying (OOK), asymmetrically-clipped optical orthogonal frequency-division multiplexing (ACO-OFDM), or asymmetrically-clipped optical Hadamard-coded modulation (ACO-HCM).

The advantage of our approach is its generality and wide applicability: In principle, realistic channel impulse responses – and based on these, realistic BER predictions – can be obtained for arbitrary rooms (for which a corresponding 3D model is available), for customized positions of luminaires and optical receivers, and for basically all practically relevant optical modulations schemes.

Assuming intensity modulation, our approach allows us to start from accurate channel models for dispersive OWC channels (in concrete geometrical settings) and directly employ them for corresponding BER simulations. To this end, we suggest to start with OWC channel modeling in the FD, because then an infinite series of diffuse reflections of any order can be considered. A TD approach would also possible, however, but is less elegant and also less accurate. The main contributions of the paper can be summarized as follows:

- With regard to a consistent framework, the importance of proper power normalization of the multipath components is pointed out, as otherwise numerically wrong BER simulation results would be produced.
- The optical channel model is embedded in an end-to-end electrical channel model suitable for intensity-modulation/direct detection schemes under linear operation.
- We confirm that the widely employed exponential model for the diffuse channel components is, in fact, relatively accurate for low bit rates, but it tends to be inaccurate for higher bit rate.
- To considerably improve simulation time, a so-called chip-rate model is presented.
- Based on the proposed modeling approach of dispersive channels, BER simulations are performed for OOK, ACO-OFDM, and ACO-HCM, and a rigorous comparison is presented, which is only possible within our consistent framework. In particular, we find that OOK in conjunction with suitable equalization at the receiver offers a quite robust performance, even if the bit rate exceeds the 3-dB bandwidth of the optical channel. Furthermore, ACO-OFDM and ACO-HCM tend to perform well for lower bit rates, but are found to be more sensitive for larger bit rates.

The remainder of the paper is organized as follows: Section II provides fundamentals of OWC channel modeling in the TD and introduces the end-to-end electrical channel model. Realistic FD-based modeling of dispersive OWC channels is introduced in Section III. In Section IV, the chip-rate model is provided, which simplifies channel emulation on digital computers and eases overall system evaluation. In Section V, BER simulations are presented for selected modulation schemes. Finally, conclusions are drawn in Section VI.

Notation: Throughout, time-domain signals and impulse responses are denoted by lower-case symbols with variable t, while associated frequency responses are denoted by corresponding upper-case symbols with variable f. Vectors and matrices are denoted by bold-faced lower-case and bold-faced upper-case letters, respectively. Finally, $*$ denotes linear convolution, and $(.)^*$ represents complex conjugation.

II. Characterization of Dispersive Optical Wireless Channels

A. Generic Modeling of the Optical Wireless Channel

We now consider an OWC channel with intensity modulation at the transmitter (Tx) side and direct detection at the receiver (Rx) side (IM/DD). This means that the information-carrying signal is the time-variant optical power $\phi(t)$ with $\mathrm{E}\{\phi(t)\} = \Phi$, where $\mathrm{E}\{.\}$ denotes expectation. The optical-to-electical conversion (O/El) at the receiver is characterized by the responsivity r of the photodiode, leading to an electrical current given by $x(t) = r\,\phi(t)$. For the ease of exposition, direct-current (DC) components are neglegted throughout this paper, since they are only relevant for the lighting function, but do not contribute to the actual data transmission. Whenever it is necessary to distinguish between the Tx and Rx optical power, we write $\phi_{\mathsf{Tx}}(t)$ and $\phi_{\mathsf{Rx}}(t)$, respectively, and use the same subscripts for their averages. These are related by

$$\Phi_{\mathsf{Rx}} = \eta \cdot \Phi_{\mathsf{Tx}}\,, \tag{1}$$

where η is the optical path loss factor. If an optical receive filter is employed, for instance a blue filter, η will also include the corresponding filter transmission loss and a possible suppression factor due to wavelength-selective filtering [3]. Within the scope of this paper, we will focus on the optical path loss, however. The channel impulse response denoted by $c(t)$ is then normalized in such way that

$$\phi_{\mathsf{Rx}}(t) = \eta \cdot c(t) * \phi_{\mathsf{Tx}}(t) \tag{2}$$

holds for the noiseless case, both for LOS as well as non-line-of-sight (NLOS) propagation. It follows that the average Rx power is given by

$$\begin{aligned}\Phi_{\mathsf{Rx}} &= \eta \int_0^\infty c(t')\mathrm{E}\{\phi_{\mathsf{Tx}}(t-t')\}\mathrm{d}t' \\ &= \eta \int_0^\infty c(t')\mathrm{d}t' \cdot \mathrm{E}\{\phi_{\mathsf{Tx}}(t)\} \\ &= \eta \cdot C(0) \cdot \Phi_{\mathsf{Tx}}\,,\end{aligned}$$

where

$$C(f) = \int_0^\infty c(t) \mathrm{e}^{-j2\pi f t} \mathrm{d}t \tag{3}$$

is the frequency response of the optical channel. Comparing this with (1) yields $C(0) = 1$. We note that because $c(t) \geq 0$ holds, this factor equals to the 1-norm of the channel impulse response, i.e.

$$\|c\|_1 = \int_0^\infty c(t) \mathrm{d}t = 1\,. \tag{4}$$

It should be emphasized that the above normalization arises naturally from the properties of optical IM/DD channels. This is a fundamental difference to radio channels which are reasonably normalized by squared quantities. This difference results in correspondingly different criteria in the evaluation of power efficiency. We briefly discuss these items.

For radio transmission, the cost is characterized by the electrical power P per bit rate R_b, which equals the energy per bit, $E_\mathsf{b} = P/R_\mathsf{b}$. The bit error rates are functions of E_b/N_0, where the one-sided noise density N_0 is of dimension $[N_0] = \mathrm{W/Hz}$. In [16], the relation

$$\frac{E_\mathsf{b}}{N_0} = \kappa \frac{(r\Phi)^2}{N_\mathsf{i} R_\mathsf{b}} \tag{5}$$

was derived for the OWC channel, where N_i is the one-sided spectral density of the noise current and has dimension $[N_\mathsf{i}] = \mathrm{A}^2/\mathrm{Hz}$, and the spectral shaping gain factor is defined by

$$\kappa := \frac{\mathrm{E}\{x^2(t)\}}{\mathrm{E}\{x(t)\}^2}\,. \tag{6}$$

In our analysis, we assume a signal-independent white Gaussian noise current at the receiver [1, Ch. 3.7]. Typically, the noise process is dominated by thermal noise and shot noise. Thermal noise is signal-independent and Gaussian, whereas shot noise is generally signal-dependent and non-Gaussian [17]. However, in the presence of strong ambient light sources (e.g., additional unmodulated luminaires or natural illumination through windows), the overall noise current can be approximated as signal-independent and Gaussian-distributed, as pointed out for instance in [18].

Note that according to (5), the *squared* optical power per bit rate is the relevant quantity. It is thus reasonable to draw BER curves as a function of $(r\Phi)^2/(N_\mathsf{i} R_\mathsf{b})$ as it is in done for the simulations shown in Section V.

Dispersive IM/DD channels require some further considerations, see Fig. 1. The upper part shows the real physical situation. The optical Tx signal $\phi_{\mathsf{Tx}}(t)$ with average power Φ_{Tx} passes the linear dispersive optical channel described by the frequency response $C(f)$. For convenience, the path loss η is allocated to a separate block. The attenuated signal $\phi(t) = \eta\phi_{\mathsf{Tx}}(t)$ passes the dispersive channel that produces the output $c(t) * \phi(t)$, which is then converted to the current

$$rc(t) * \phi(t) = c(t) * x(t) \tag{7}$$

with $x(t) = r\,\phi(t)$. This signal is corrupted by the white noise current $w(t)$ of spectral density N_i, which yields the additive

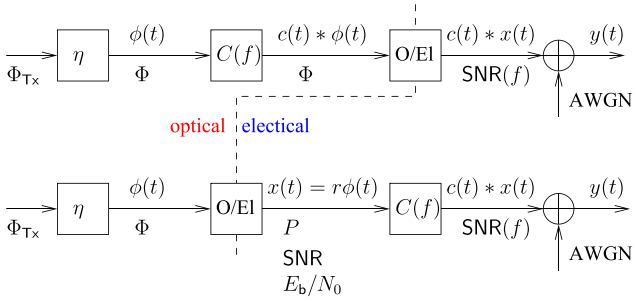

Fig. 1. Block diagram for the optical dispersive IM/DD channel.

white Gaussian noise (AWGN) channel

$$y(t) = c(t) * x(t) + w(t)\,. \tag{8}$$

Since all the signals in the above equation are electrical currents, it is convenient to analyze the channel in the electrical domain as depicted in the lower part of the figure. One may freely interchange the order of the optical-to-electical conversion (multiplication by r) and the dispersive channel (convolution with $c(t)$). This means that the dispersive channel is completely shifted into the electrical domain. Its input signal $x(t)$ has an electrical power proportional to $\mathrm{E}\{x^2(t)\}$ which is related to the optical power by

$$\mathrm{E}\{x^2(t)\} = \kappa(r\Phi)^2\,, \tag{9}$$

which leads to (5). Note that even though the channel is analyzed in the electrical domain, the cost is characterized by the optical power Φ and not by the electrical power P. This must be taken into account by drawing the BER curves as function of $\frac{(r\Phi)^2}{N_\mathsf{i} R_\mathsf{b}}$ rather than of E_b/N_0. The electrical energy per bit, E_b, includes the path loss, but not the dispersion of the optical channel. This quantity is convenient for the analysis and the simulation, but it has no direct physical interpretation. Neither has the electrical signal to noise ratio (SNR) defined as

$$\mathsf{SNR} := \frac{\mathrm{E}\{x^2(t)\}}{N_\mathsf{i} B_\mathsf{n}} = \kappa \frac{(r\Phi)^2}{N_\mathsf{i} B_\mathsf{n}}\,, \tag{10}$$

where B_n denotes the electrical noise bandwidth. Note that the nominator in this fraction is defined before the input of the dispersive channel, and the denominator only after it. The above quantity can be interpreted as a kind of transmitter SNR for a path loss normalized to $\eta = 1$. In particular for the performance analysis of multi-carrier modulation it is meaningful to define a frequency-dependent SNR given by

$$\mathsf{SNR}(f) = |C(f)|^2\,\mathsf{SNR} \tag{11}$$

to describe the SNR in each subcarrier and to evaluate the error rate there.

B. Characteristic Parameters of the Optical Wireless Channel

We observe that $c(t)$ together with (4) characterizes a normalized power-delay profile because

$$\int_{t_1}^{t_2} c(t) \mathrm{d}t \tag{12}$$

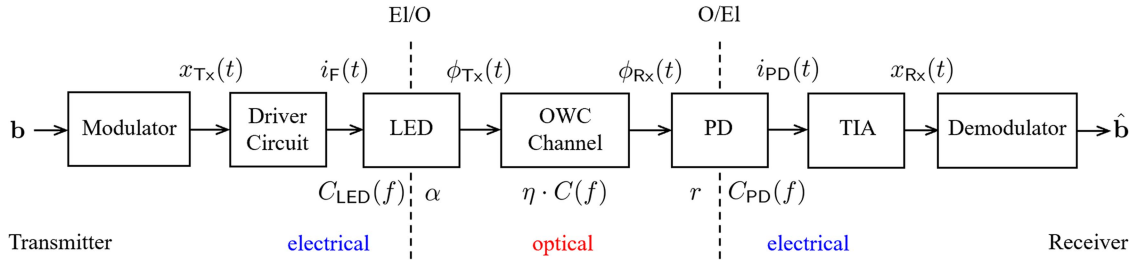

Fig. 2. End-to-end system model including the transmitter-sided LED, the OWC channel, and the receiver-sided PD.

is the relative amount of power between the delay times t_1 and t_2, see (4). It thus appears natural to define the optical mean delay as

$$\mu_{\mathsf{opt}} := \int_0^\infty t c(t) \mathrm{d}t \tag{13}$$

and the optical root mean square (RMS) delay spread as

$$\sigma_{\mathsf{opt}} := \left(\int_0^\infty (t - \mu_{\mathsf{opt}})^2 c(t) \mathrm{d}t \right)^{1/2}. \tag{14}$$

This appears more appropriate to the physical situation than the established definitions [14], [19] that work with $c^2(t)$ rather than with $c(t)$. In this context it should be pointed out that $c(t)$ *must* have the dimension $[c(t)] = \mathrm{s}^{-1}$ because the channel does not change the dimension of the optical power at the input. One can easily check that

$$\|c\|_2 = \sqrt{\int_0^\infty |c(t)|^2 \mathrm{d}t} \tag{15}$$

then has the dimension $\sqrt{\mathrm{s}^{-1}}$, and this *forbids* to normalize $\|c\|_2$ to one in the case of an OWC channel. Note that in channel modeling for radio transmission, it is customary to use the $\|\cdot\|_2$-norm for channel impulse response normalization, which is justified since all transmitted and received signals are electrical-domain signals (i.e., voltage signals in baseband or bandpass domain). In the case of a dispersive OWC channel, however, the physical transmitted and received signals are optical-domain (i.e., power) signals, which renders the $\|\cdot\|_1$-norm to be the relevant norm for channel impulse response normalization.

C. End-to-End Electrical Channel Model

The general OWC channel model defined above can be tailored to specific electronic devices employed at the transmitter side (for IM) and the receiver side (for DD). Within the scope of this paper, we will focus on light-emitting diodes (LEDs) at the transmitter side and a corresponding photodetector (PD) at the receiver side, as already introduced in Section II-A.

The end-to-end system model is depicted in Fig. 2. A detailed discussion is provided in Appendix A. If transmitter and receiver are both operated in the linear regime, we arrive at an all-electrical end-to-end channel model, which includes the *optical* channel impulse response $c(t)$ as a core component:

$$x_{\mathsf{Rx}}(t) = c_{\mathsf{el,ov}}(t) * x_{\mathsf{Tx}}(t), \tag{16}$$

where

$$c_{\mathsf{el,ov}}(t) = r \cdot \eta \cdot \alpha \cdot c_{\mathsf{LED}}(t) * c(t) * c_{\mathsf{PD}}(t). \tag{17}$$

This enables realistic BER predictions for all practically relevant optical modulation schemes, provided that the frequency responses $C_{\mathsf{LED}}(f)$ and $C_{\mathsf{PD}}(f)$ of the LED and the PD are known and the frequency response $C(f)$ of the OWC channel is precisely modeled. This includes corresponding signal processing steps, in order to tailor the (overall) channel impulse response to a desired discrete time grid, as detailed in Section III.

Note that if the linearity assumption is violated at the transmitter side, it may still be possible to simulate the optical signal $\phi_{\mathsf{Tx}}(t)$ for a given transmitted bit sequence $\mathbf{b}$. In this case, the above channel model may be reduced to

$$x_{\mathsf{Rx}}(t) = c_{\mathsf{ov}}(t) * \phi_{\mathsf{Tx}}(t), \tag{18}$$

where

$$c_{\mathsf{ov}}(t) = r \cdot \eta \cdot c(t) * c_{\mathsf{PD}(t)}, \tag{19}$$

which still allows a BER prediction for the specific bit sequence $\mathbf{b}$.

III. Realistic Modeling of Dispersive Optical Wireless Channels

In the following, we propose a method for realistic modeling of the optical channel impulse response $c(t)$. For the ease of exposition, we will disregard the spectral characteristics of the LED and the PD in the sequel, i.e., $C_{\mathsf{LED}}(f) = C_{\mathsf{PD}}(f) = 1$. Based on Section II-C, a generalization is straightforward, however.

A. Frequency-Domain Optical Wireless Channel Emulation Revisited

In this subsection, we briefly summarize the FD approach for the emulation of optical wireless indoor channels that will be used in this paper. We use the term *emulation* for the deterministic modeling of the channel and speak of *simulation* only in the context of random processes.

The basic idea is that irradiance on the walls and objects inside a room (or any cavity) can approximately be described by the discrete recursive irradiance equation [8], [11]

$$\mathbf{u} = \mathbf{g} + \mathbf{K}\mathbf{u}\,, \tag{20}$$

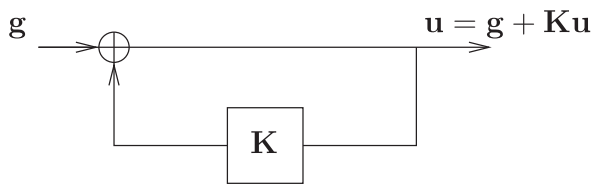

Fig. 3. Irradiance inside a room or cavity can be described as a recursive system.

which is visualized in Fig. 3. The surfaces are divided into tiles and discretized, and the vector $\mathbf{u}$ with elements u_i corresponding to tile number i describes the irradiance on the walls. The vector $\mathbf{g}$ describes the links from the source to the tiles, and the matrix $\mathbf{K}$ with elements K_{ik} describes the light propagation from all tiles k to i, thereby including their reflectivity factors. Equation (20) has the same structure as the discrete radiosity equation that is well known in computer graphics [20], [21], and like this, it can be derived as a discrete approximation from an integral equation. For the analysis of optical indoor channels, the irradiance is more convenient than the radiosity. The idea of the FD approach described in [8], [11] is to consider not only the optical link budget from the source to each tile, but also the corresponding time delay (which is not relevant in computer graphics). This leads to the interpretation of u_i as a transfer function for the optical link from the source to tile number i. The linear system of equations in (20) can be solved using standard methods, and the complete transfer function for the diffuse link from the source to the receiver (Rx) can then be obtained by adding a final rendering step for the links from all tiles to the Rx.

Like in the radiosity approach, the discrete approximation can be performed in a very simple way by considering only the central point of each tile [8]. A more accurate approach is the finite element method (FEM), which is state of the art in the field of realistic image synthesis, see e.g. [21] and the references therein. This method was taken up in [11] and adapted for optical wireless indoor channels by writing the elements of the matrix $\mathbf{K}$ as

$$K_{ik} = \mathrm{e}^{-j2\pi f \tau_{ik}} L_{ik} \rho_k \,, \tag{21}$$

where f denotes the frequency variable, τ_{ik} is the contribution to the propagation delay corresponding to the way from tile k to tile i, and ρ_k is the reflectivity factor of tile k. The *form factor*

$$L_{ik} = \frac{1}{A_k} \int_{\mathcal{A}_i} \int_{\mathcal{A}_k} L(\mathbf{x}, \mathbf{x}') \mathrm{d}A(\mathbf{x}') \mathrm{d}A(\mathbf{x}) \tag{22}$$

describes the radiation transfer from surface element (tile) $\mathcal{A}_k$ with area A_k to surface element $\mathcal{A}_i$, and $L(\mathbf{x}, \mathbf{x}')$ is the Lambert propagation kernel. These form factors are either analytically known from the theory of heat transfer [22], [23] or can be calculated numerically in advance. It should be emphasized that the FEM approach [11] provides a much higher accuracy compared to the simple approach [8] at the same computational complexity.

B. Generating Channels for Performance Simulations

This subsection describes the signal processing to obtain discrete-time impulse responses suitable for BER simulations from arbitrary frequency responses generated by FEM calculations [11]. All numerical results correspond to the *diffuse* non-line-of-sight (NLOS) component of the Barry A channel [24].

1) Frequency and Impulse Response of the Channel: The methods described in [8], [11] calculate a frequency response for a certain frequency spacing Δf at frequencies

$$f_k = k\Delta f \;\text{ with } k = 0, 1, \ldots, N_{\mathsf{FFT}}/2 \,, \tag{23}$$

where the fast Fourier transform (FFT) length N_{FFT} has been chosen to be even. These calculations yield the full frequency response $C_\eta(f) = \eta C(f)$ including the path loss, but in the following discussion, we consider the quantity $C(f)$ normalized to $C(0) = 1$. We write

$$C[k] = C(f_k) \text{ with } k = 0, 1, \ldots, N_{\mathsf{FFT}}/2 \tag{24}$$

for these values. Because the impulse response $c(t)$ must be real valued, the frequency response for negative frequencies can be obtained from the property

$$C(-f) = C^*(f) \,. \tag{25}$$

The discrete frequency response for the negative frequencies is denoted thus given by

$$C[N_{\mathsf{FFT}} - k] = C^*[k] \text{ for } k = 1, \ldots, N_{\mathsf{FFT}}/2 - 1 \,. \tag{26}$$

The sampling frequency for the system is given by

$$f_{\mathsf{s}} = N_{\mathsf{FFT}} \Delta f \,, \tag{27}$$

and $f_{\mathsf{s}}/2$ is the simulation bandwidth. The discrete impulse response $c[n]$ is calculated by means of the inverse FFT (IFFT). Before doing this, $C[k]$ must be windowed in order to reduce leakage. We choose a window that is flat inside half the simulation bandwidth (i.e. between 0 and $f_{\mathsf{s}}/4$) and shows a smooth raised cosine decay from there to $f_s/2$. We point out that the sampling frequency must be chosen high enough and that all relevant signal components must be in the range between 0 and $f_{\mathsf{s}}/4$. The physical impulse response $c(t)$ of dimension 1/seconds calculated (approximately) in this way for the time raster $t_{\mathsf{s}} = 1/f_{\mathsf{s}}$ is given by

$$c(nt_{\mathsf{s}}) = \frac{1}{t_{\mathsf{s}}} c[n] \,. \tag{28}$$

Note that resampling of $c[n]$ to a different, e.g., finer grid is possible by means of standard digital signal processing steps.

2) The Exponential Model: The diffuse NLOS part of the indoor channel impulse response typically shows an exponential decay as the asymptote. This can physically be explained by the multiple reflections at the walls and a propagation loss that is related to the geometrical series [25]. The diffuse impulse response can thus often be modeled as

$$c_{\mathsf{exp}}(t) = \frac{1}{\tau} \mathrm{e}^{-(t-t_0)/\tau} \Theta(t - t_0) \,, \tag{29}$$

where τ is the time constant of the exponential decay, t_0 is an overall delay, and $\Theta(t)$ denotes the Heaviside function. If a direct

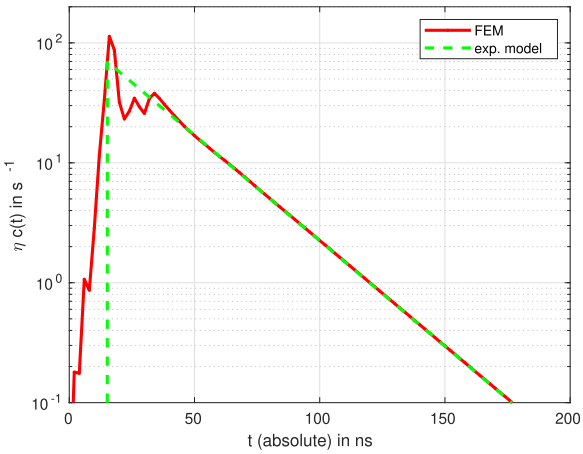

Fig. 4. Impulse response $\eta c(t)$ (on a log scale) obtained from the FEM calculations for $f_s = 500$ MHz. The theoretical impulse response (29) of the exponential model is drawn in green.

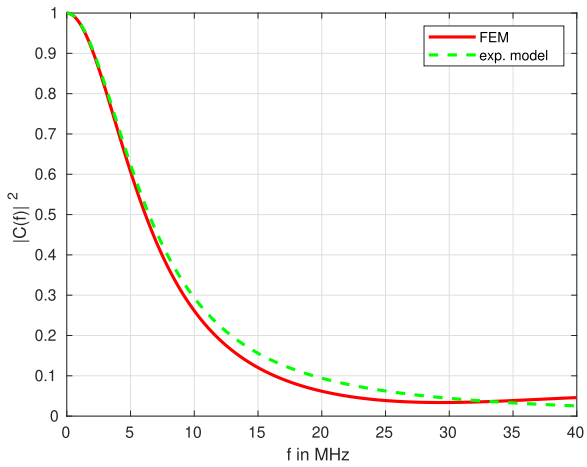

Fig. 5. Frequency response obtained from the FEM simulations. The theoretical frequency response (30) of the exponential model is drawn in green.

TABLE I
PARAMETERS OBTAINED FROM LINEAR REGRESSION FOR THE ASYMPTOTE

τ	24.7 ns
$c_0\tau$	7.41 m
$f_{3\mathrm{dB}} = (2\pi\tau)^{-1}$	6.45 MHz
t_0	15 ns
$c_0 t_0$	4.5 m

LOS link with delay time t_{LOS} is existent, the impulse response of (29) must be superposed with $\delta(t - t_{\mathsf{LOS}})$ and properly chosen weighting factors. Since the time decay of the impulse response determines the low-frequency characteristics of the frequency response, it can thus often be assumed that the diffuse channel within e.g. the 3 dB bandwidth can approximately be described by the frequency response [26]

$$C_{\mathsf{exp}}(f) = \frac{\mathrm{e}^{-j2\pi f t_0}}{1 + j2\pi f\tau}\,, \tag{30}$$

which corresponds to the impulse response (29). If a direct LOS link with delay time t_{LOS} is existent, the frequency response of (30) must be superposed with $\exp(-j2\pi f t_{\mathsf{LOS}})$.

The time constant τ and the overall delay t_0 can be calculated from the impulse response by linear regression. For the diffuse component of the Barry A channel [24], in Fig. 4 the impulse response obtained from FEM calculations is shown together with the exponential asymptote calculated by linear regression. The values obtained for τ and t_0 are listed in Table I. The corresponding frequency responses are shown in Fig. 5. We observe that the curve of the exponential model agrees quite well to the FEM calculations within the 3 dB bandwidth. The discrete impulse responses to be used for simulations are shown in Fig. 6. Both have been generated in the same way from the corresponding frequency response via IFFT. We notice that there are negative precursors to the main peak of the signal. They are due to the bandwidth reduction introduced by the FD windowing step described above and can be interpreted as a result of lowpass

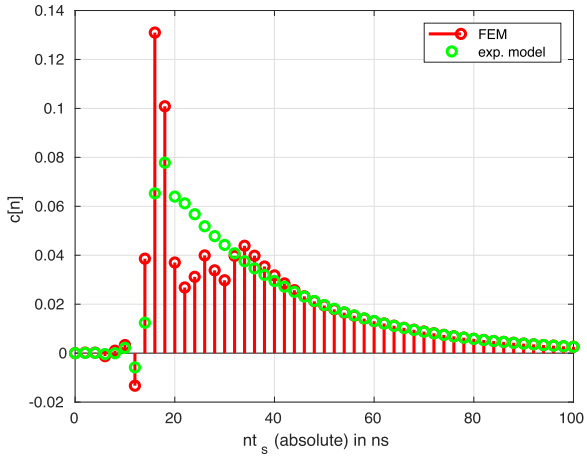

Fig. 6. Impulse response for simulations obtained from the FEM calculations for $f_s = 500$ MHz. The theoretical impulse response (29) of the exponential model is drawn in green.

filtering in the electrical domain. For the considered example, the passband of this induced lowpass filter spans the frequency range between 0 Hz and... 125 MHz ($= f_s/4$), which is wider than typical electrical bandwidths of practical LEDs and PDs and therefore does not have any consequence with regard to the end-to-end electrical channel model. Note that these impulse responses are normalized to the optical power one, i.e.

$$\sum_{n=0}^{N_{\mathsf{FFT}}-1} c[n] = 1\,. \tag{31}$$

3) Extension to Multiple-Input Multiple-Output Settings: The frequency response $C(f)$ and thus the impulse response $c(t)$ of the OWC channel depends on the geometry of the considered room and the positions of the LED and the PD – via the matrix $\mathbf{K}$ in (20) and the final rendering step. Our modeling procedure can therefore readily be extended to multiple-input multiple-output (MIMO) settings with multiple (M) LEDs at the Tx side and/or multiple (N) PDs at the Rx side, by emulating a separate

impulse response $c_{\mu,\nu}(t)$ for each LED-PD pair ($\mu = 1, .., M$, $\nu = 1, .., N$). In particular, if all LEDs emit the same signal $x_{\mathsf{Tx}}(t)$ (e.g., for extending the coverage), the effective impulse response for the ν-th PD is given by

$$c_{\mathsf{eff},\nu}(t) = \sum_{\mu=1}^{M} c_{\mu,\nu}(t)\,. \tag{32}$$

($1 \le \nu \le N$). A numerical example for a specific indoor scenario can be found in [8].

IV. Chip-Rate Model

In this subsection we show how the Forney formalism [27], [28] can be applied to optical channels obtained by the method described above to obtain a chip-rate model suitable for fast simulations. We introduce the term *chip* for a common treatment of OOK and ACO-HCM (and similar intensity modulation schemes). For OOK, a chip simply corresponds to a symbol that is turned on or off. For ACO-HCM, a symbol vector consists of N chips that can take a set of discrete values dependent on the modulation. The sampling rate for the channels obtained in Section III is usually much higher that the chip-rate of the modulation scheme. We show how to proceed, without loss of precision, from the matched filter (MF) outputs of the quasi-continuous channel model to a discrete-time channel model.

A. Signal Shapes, Notation, and Electrical Power Loss

Let us now consider chip pulses resulting from a pulse shaping filter $S(f)$ normalized to $S(0) = 1$. More specifically, we consider rectangular pulses with period T_{c} that may either be symmetric to the origin or causal, i.e.

$$S(f) = \mathrm{sinc}(fT_{\mathsf{c}}) \text{ or } S(f) = \mathrm{sinc}(fT_{\mathsf{c}}) \cdot \mathrm{e}^{-j2\pi fT_{\mathsf{c}}/2}\,. \tag{33}$$

We note that for this pulse, the normalization

$$\int_{-\infty}^{\infty} |S(f)|^2 \mathrm{d}f = \frac{1}{T_{\mathsf{c}}} \tag{34}$$

holds. The total transfer function of the pulse shaping $S(f)$ and the optical channel $C(f)$ discussed in Section II is then given by

$$H(f) = C(f)S(f)\,. \tag{35}$$

(For the ease of exposition, we set $C_{\mathsf{LED}}(f) = C_{\mathsf{PD}}(f) = 1$.) We note that because $C(0) = 1$ and $S(0) = 1$, this channel is normalized to $H(0) = 1$ as well. In the discrete time domain, this leads to

$$\sum_n s[n] = 1 \text{ and } \sum_n h[n] = 1 \tag{36}$$

for the corresponding samples. The electrical energy loss due to the dispersive optical channel is described by the electrical channel gain factor

$$\Gamma := \frac{\sum_n |h[n]|^2}{\sum_n |s[n]|^2}\,. \tag{37}$$

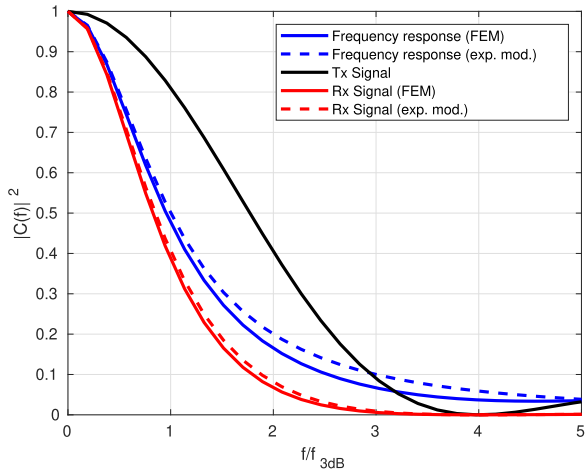

Fig. 7. Spectral shapes of the signals and the channel in the electrical domain for Barry A (diffuse) and $f_{3\,\mathrm{dB}}T_{\mathsf{c}} = 4$: FEM and exponential model.

This can equivalently be expressed in the frequency domain by

$$\Gamma = \frac{\int_{-\infty}^{\infty} |H(f)|^2 \mathrm{d}f}{\int_{-\infty}^{\infty} |S(f)|^2 \mathrm{d}f} = T_{\mathsf{c}} \int_{-\infty}^{\infty} |H(f)|^2 \mathrm{d}f\,, \tag{38}$$

where (34) has been used to obtain the last expression. The spectral shape $|C(f)|^2$ of the dispersive channel deforms the signal, as shown in Fig. 7 for the considered example (Barry A diffuse) and $f_{3\,\mathrm{dB}}T_{\mathsf{c}} = 4$ (with $f_{3\,\mathrm{dB}}$ as given in Table I). The factor $\Gamma < 1$ that characterizes the deformation can be visualized as the ratio between the area under curve for the Rx signal (red) and the area under the curve for the Tx signal (black) in Fig. 7. This electrical power loss cannot be recovered at the receiver. Looking at the figure, it becomes intuitively evident that the signal bandwidth should not exceed the channel bandwidth too much in order not to lose too much signal energy. Translating this to the time domain leads to the property that the impulse response $h[n]$ will not become much longer than the chip duration. Thus, the lowpass characteristics of the channel rather the length of the time dispersion limits the system. This is in contrast to what is familiar from mobile radio channels.

B. Sampling Rate Reduction

The discrete signals in the treatment given above are equivalent to the corresponding continuous signals because Nyquist sampling is applied. Integrals are equivalent to sums, and continuous filters can be replaced by discrete filters. We may thus speak of *quasi-continuous* signals. In the next step, the quasi-continuous MF outputs[1] $h^*[-n] * h[n]$ will be down-sampled to arrive at a chip-rate model for the overall channel. The normalized quasi-continuous autocorrelation function (ACF) is given by

$$R_{hh}[n] = \frac{h^*[-n] * h[n]}{\sum_n |s[n]|^2}\,. \tag{39}$$

[1]We write $h^*[n]$ even though the signal is real-valued.

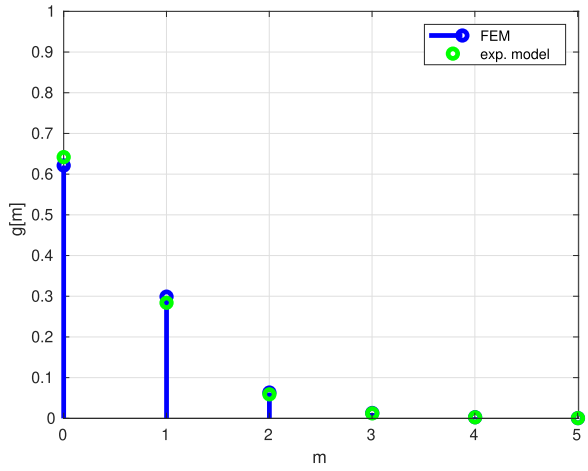

Fig. 8. Discrete chip-rate model impulse responses for Barry A (diffuse) and $f_{3\,\mathrm{dB}}T_\mathrm{c} = 4$: FEM and exponential model.

Obviously, this is normalized to $R_{hh}[0] = \Gamma$. Note that $R_{hh}[n] = R_{hh}^*[-n]$. The down-sampled chip clock ACF is given by

$$\tilde{R}_{hh}[m] = R_{hh}[mL] = \frac{\int_{-\infty}^{\infty} |H(f)|^2 \mathrm{e}^{j2\pi m f T_\mathrm{c}} \mathrm{d}f}{\int_{-\infty}^{\infty} |S(f)|^2 \mathrm{d}f} \,. \tag{40}$$

Typically, only very few samples of this discrete ACF are relevant because the others are close to zero.

C. Factorization and Decorrelation

We now apply the Forney formalism [27], [28] for channels with ISI and consider the z-transform

$$\tilde{R}_{hh}(z) = \sum_{m=-M}^{M} \tilde{R}_{hh}[m] z^{-m} \tag{41}$$

of the relevant coefficients with $m = 0, \pm 1, \ldots \pm M$. The analysis of the zeros leads to a factorization

$$\tilde{R}_{hh}(z) = G(z) G^*(1/z^*) \,. \tag{42}$$

This eventually yields the coefficients $g[m]$ of

$$G(z) = \sum_{m=0}^{M} g[m] z^{-m} \,. \tag{43}$$

The discrete chip-rate model impulse responses for the considered example (Barry A diffuse, NLOS setting) and $f_{3\,\mathrm{dB}}T_\mathrm{c} = 4$ are depicted in Fig. 8. The whitening (decorrelation) filter is given by $1/G(z)$. We should note that $1/G(z)$ describes an infinite-impulse response (IIR) filter and can be approximately described by a finite-impulse response (FIR) filter. The discrete chip-rate model can then be written as [28], [1, Fig. 3.9]

$$y[m] = g[m] * x[n] + w[m] \,, \tag{44}$$

where $x[m]$ is the input (chip) sequence, and $w[m]$ is the discrete-time real-valued AWGN with

$$\mathrm{E}\{w[m] w[m']\} = \frac{N_0}{2} \delta[m - m'] \,. \tag{45}$$

D. Normalization of the Discrete Impulse Response

Recall that the z-values on the unit circle are related to the frequency f by

$$z = \mathrm{e}^{j2\pi f T_\mathrm{c}} \,, \tag{46}$$

and $f = 0$ corresponds to $z = 1$. For these z-values with $|z| = 1$ on the unit circle, the z-transform of the sampled ACF is given as the periodic continuation

$$\tilde{R}_{hh}(z) = \sum_{k=-\infty}^{\infty} |H(f - k/T_\mathrm{c})|^2 \,. \tag{47}$$

From (35) it follows that

$$H(k/T_\mathrm{c}) = \delta[k] \tag{48}$$

holds, which leads to

$$\tilde{R}_{hh}(1) = |H(0)|^2 = 1 \,. \tag{49}$$

From (42) and (43) we conclude

$$\sum_{m=0}^{M} g[m] = G(1) = 1 \,. \tag{50}$$

The above $\|\cdot\|_1$-normalization of the discrete channel impulse response is in the end a consequence of the normalization $C(0) = 1$ for the frequency response of the optical channel. This is very different from the usual $\|\cdot\|_2$-normalization for radio channels. The interpretation of the $\|\cdot\|_2$-norm for optical channels can be obtained as follows. We recall that

$$g^*[-m] * g[m] = \tilde{R}_{hh}[m] \tag{51}$$

holds, and in particular

$$\tilde{R}_{hh}[0] = \sum_{m} |g[m]|^2 \,. \tag{52}$$

From (38) and (40) we conclude that the electrical gain factor Γ is just the $\|\cdot\|_2$-norm of the optical channel:

$$\Gamma = \|g\|_2 = \sum_{m} |g[m]|^2 \,. \tag{53}$$

For the example given by Figs. 7 and 8, the gain factor calculated by the above formula is $\Gamma = -3.2\,\mathrm{dB}$ for the FEM channel and $\Gamma = -3.0\,\mathrm{dB}$ for the exponential model.

The above discussion can be summarized as follows: For optical channels, the reference quantity is the optical power, which is characterized by the 1-norm. The electrical power is characterized by the 2-norm, which follows from the channel properties as a secondary quantity.

V. Bit Error Rate Simulations

In this section, we show examples for BER simulations with a dispersive OWC channel generated by FEM calculations as described above. In particular, the chip-rate model introduced in Section IV is employed for OOK (Section V-A) and ACO-HCM (Section V-C).

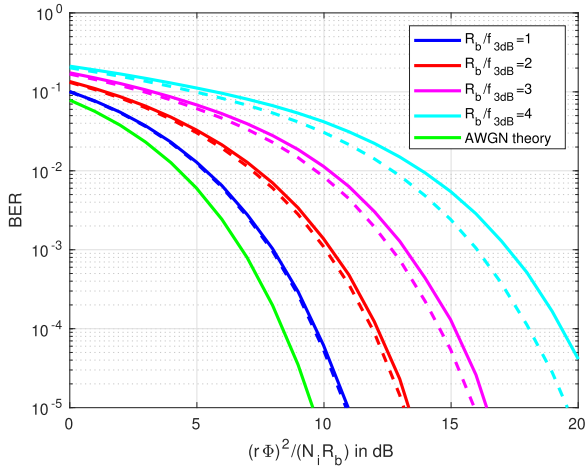

Fig. 9. BER simulations for OOK-NRZ and the channel for Barry A (diffuse) with and $f_{3\,\mathrm{dB}}T_\mathrm{c} = 1, 2, 3, 4$: FEM (solid lines) and exponential model (dashed lines).

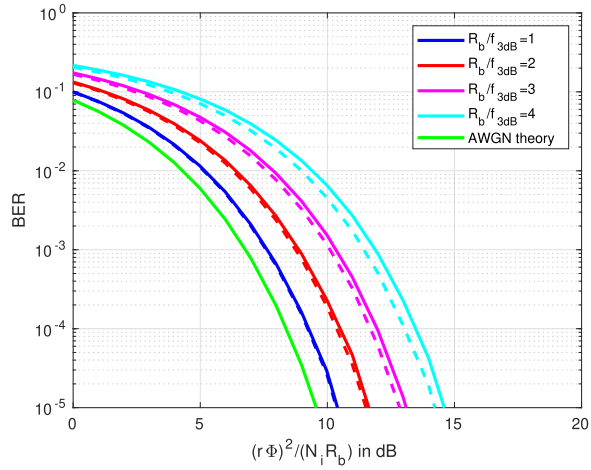

Fig. 10. BER simulations for OOK-NRZ with ZFE and the channel for Barry A (diffuse) with and $f_{3\,\mathrm{dB}}T_\mathrm{c} = 1, 2, 3, 4$: FEM (solid lines) and exponential model (dashed lines).

A. BER Simulations for OOK

As a first example, simple modulation by OOK with non-return-to-zero rectangular pulses (OOK-NRZ) is considered. The signal is either turned on or off during the period T_c, and the bit rate is given by $R_\mathrm{b} = 1/T_\mathrm{c}$. Results for BER simulations with increasing dispersion characterized by $f_{3\,\mathrm{dB}}T_\mathrm{c} = 1, 2, 3, 4$ (with $f_{3\,\mathrm{dB}}$ as given in Table I) are shown in Fig. 9. The theoretical bit error probability [16]

$$P_\mathrm{b} = \frac{1}{2}\mathrm{erfc}\left(\sqrt{\frac{(r\Phi)^2}{N_\mathrm{i}R_\mathrm{b}}}\right) \tag{54}$$

for OOK-NRZ in the non-dispersive AWGN channel is drawn in green for comparison.

These simulations show that the increasing dispersion significantly degrades the performance. Furthermore, we note that the exponential model for the diffuse channel components is relatively accurate for low $R_\mathrm{b}/f_{3\,\mathrm{dB}}$ ratios, but rather inaccurate for high $R_\mathrm{b}/f_{3\,\mathrm{dB}}$ ratios, which is due to the good match of the exponential model in the lower frequency region of $C(f)$, cf. Fig. 5. For the dispersion factor $f_{3\,\mathrm{dB}}T_\mathrm{c} = 4$ (cyan curve), which corresponds to the channel depicted in Fig. 8, the degradation is on the order of 10 dB. These degradations can be reduced by channel equalization. First we apply the zero-forcing equalizer (ZFE) as described in [28]. The ZFE simply inverts the channel by applying the impulse response $g^{-1}[m]$ corresponding to $G^{-1}(z) = 1/G(z)$ to the channel given by (44). The decisions are made for the Rx symbols $g^{-1}[m] * y[m]$. Simulation results for the same channels as above are shown in Fig. 10. We observe significant improvement because the dispersion is completely removed by this equalizer. However, it it well known that the ZFE suffers from noise enhancement at the frequencies with small channel amplitudes. For optical channels like the one shown in Fig. 7, this is less critical than for mobile radio channels where notches with spectral zeros may occur. The problem of noise enhancement is avoidable by the maximum-likelihood sequence estimator (MLSE) [28], which finds the most probable Tx sequence. The corresponding simulations for the same channel are shown in Fig. 11. A further reduction of the BER can be observed. However, these further gains are significant only for higher dispersion values like $f_{3\,\mathrm{dB}}T_\mathrm{c} = 4$ and rather small for $f_{3\,\mathrm{dB}}T_\mathrm{c} = 1$ where ZFE and MLSE perform very similar. It is interesting to observe that the 3 dB loss for the MLSE at $f_{3\,\mathrm{dB}}T_\mathrm{c} = 4$ (cyan curve) fits quite well to the electrical power loss characterized by the value $\Gamma \approx -3\,\mathrm{dB}$ that was found above for this channel depicted in Figs. 7 and 8.

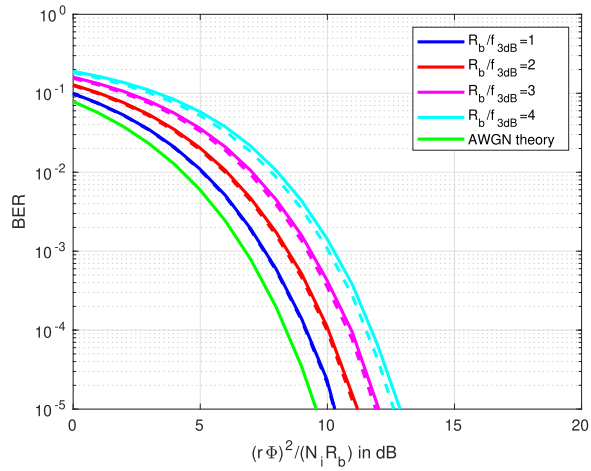

Fig. 11. BER simulations for OOK-NRZ with MLSE equalizer and the channel for Barry A (diffuse) with and $f_{3\,\mathrm{dB}}T_\mathrm{c} = 1, 2, 3, 4$: FEM (solid lines) and exponential model (dashed lines).

B. BER Simulations for ACO-OFDM

As a second example, we consider ACO-OFDM [29]. In this modulation scheme, only the odd-indexed OFDM sub-carriers

$k = 1, 3, \ldots, 2K-1$ are modulated for which the complex information symbols can be recovered from the clipped signal. The bandwidth is given by

$$B = \frac{2\,K}{T}\,, \tag{55}$$

where T is the useful OFDM symbol length and $1/T$ is the (fixed) sub-carrier spacing. At the moment, we ignore a guard interval (also called *cyclic prefix*). Using M^2-QAM modulation for each of the K occupied OFDM sub-carriers, the bit rate is given by

$$R_\mathrm{b} = \frac{K}{T}\log_2(M^2) = \frac{2\,K}{T}\log_2(M)\,, \tag{56}$$

which leads to the spectral efficiency

$$\frac{R_\mathrm{b}}{B} = \log_2 M\,. \tag{57}$$

This halving of spectral efficiency compared to classical OFDM/M^2-QAM stems from the fact that only half of the sub-carriers are permitted to be modulated. The bit error probability for OFDM/M^2-QAM in the non-dispersive optical AWGN channel is approximately given by [16]

$$P_\mathrm{b} \approx \frac{1}{\log_2 M}\frac{M-1}{M}\mathrm{erfc}\left(\sqrt{\gamma\kappa\frac{r^2\Phi^2}{N_\mathrm{i}R_\mathrm{b}}}\right), \tag{58}$$

where the shaping gain factor κ is defined by (6), and

$$\gamma = \frac{3}{2}\frac{\log_2 M}{M^2-1} \tag{59}$$

is the electrical power gain factor for ACO-OFDM/M^2-QAM, which is reduced by a factor of two compared to classical OFDM/M^2-QAM as a result of clipping loss. It can be shown [16], [29] that the shaping gain factor for ACO-OFDM is approximately given by $\kappa \approx \pi$. For a channel with frequency response $C(f)$, the electrical power for each sub-carrier number k is attenuated by a factor $|C(f_k)|^2$ with $f_k = k/T$, cf. (11). This results in the bit error probability

$$P_{\mathrm{b},k} \approx \frac{1}{\log_2 M}\frac{M-1}{M}\mathrm{erfc}\left(\sqrt{|C(f_k)|^2\gamma\kappa\frac{r^2\Phi^2}{N_\mathrm{i}R_\mathrm{b}}}\right) \tag{60}$$

for that sub-carrier. The overall bit error probability is obtained as an average over all occupied sub-carriers.

The above analytical formula can be confirmed by the following numerical simulations. We consider again the example of the diffuse Barry A channel and choose a useful symbol length of $T = 10\,\mu$s, which leads to $B = 6.4\,$MHz for $K = 32$ occupied sub-carriers. This fits quite well to the value $f_{3\,\mathrm{dB}} = 6.45\,$MHz listed in Table I. The sub-carrier positions and the frequency response are drawn in Fig. 12. We chose the high FFT length $N_\mathrm{FFT} = 5000$ corresponding to a sampling frequency $f_\mathrm{s} = N_\mathrm{FFT}/T = 500\,$kHz in order to to work with a quasi-continuous signal. The corresponding discrete-time channel impulse response is then given by Fig. 6. Looking at the figure, we see that a guard interval of length $T_\mathrm{g} = 100\,$ns, which is 1% of the useful symbol length, should be sufficient. This

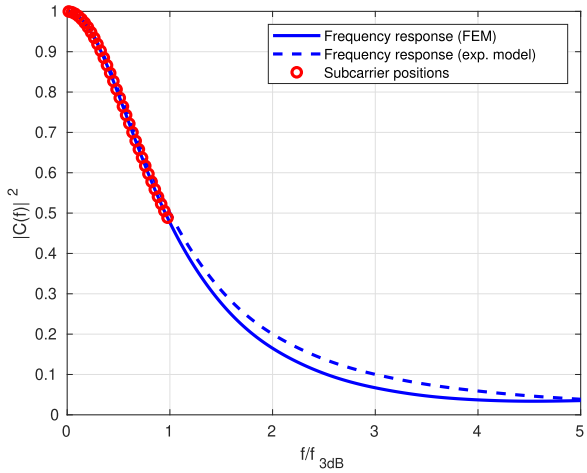

Fig. 12. Frequency response obtained from the FEM calculations and the exponential model. The positions of the occupied sub-carriers ($K = 32$) are marked by red circles.

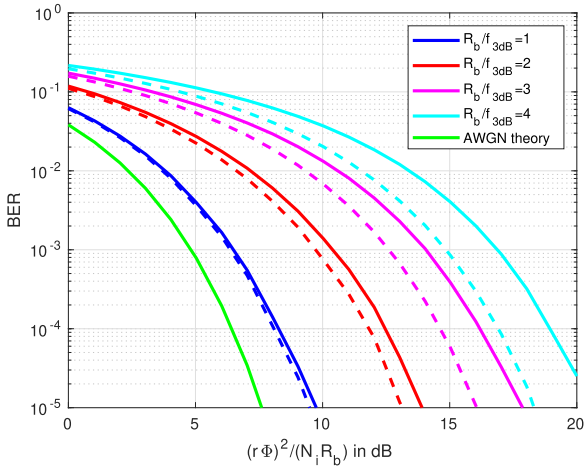

Fig. 13. BER simulations for ACO-OFDM/4-QAM in the dispersive OWC channel: FEM channel (solid lines) and exponential model (dashed). The theoretical ACO-OFDM curve for the non-dispersive (AWGN) channel is drawn as a reference.

has been verified by additional simulations. Fig. 13 shows such simulations for ACO-OFDM/4-QAM for $K = 32, 64, 96, 128$ corresponding to $R_\mathrm{b}/f_{3\,\mathrm{dB}} = 1, 2, 3, 4$. It can be observed that the benefits of ACO-OFDM compared to OOK-NRZ get lost as soon as more carriers are in the region where the channel frequency response shows a severe attenuation. This becomes obvious when comparing Fig. 13 with Fig. 9, where OOK-NRZ outperforms ACO-OFDM for bit rates $R_\mathrm{b} > f_{3\,\mathrm{dB}}$, even without any equalization. Moreover, in conjunction with an MLSE equalizer, OOK-NRZ attains a comparable BER even for $R_\mathrm{b} = f_{3\,\mathrm{dB}}$. This suggest to use a higher-level modulation scheme for ACO-OFDM in order to reduce the bandwidth. We expect a trade-off between the reduced Euclidean distance of the signal constellation an the reduced channel attenuation. Simulations for ACO-OFDM/16-QAM for $K = 16, 32, 48, 64$ corresponding to $R_\mathrm{b}/f_{3\,\mathrm{dB}} = 1, 2, 3, 4$ are shown in Fig. 14. We

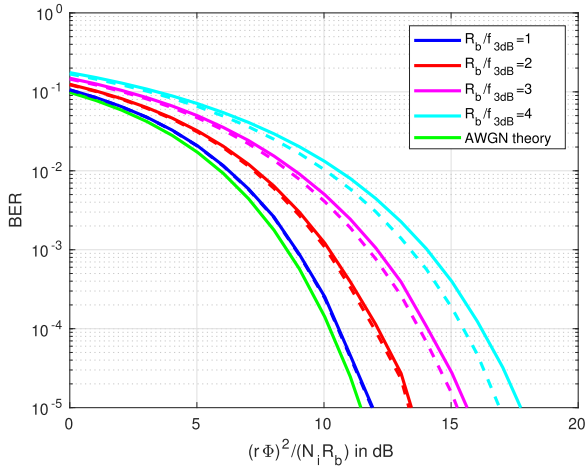

Fig. 14. BER simulations for ACO-OFDM/16-QAM in the dispersive OWC channel: FEM channel (solid lines) and exponential model (dashed). The theoretical ACO-OFDM curve for the non-dispersive (AWGN) channel is drawn as a reference.

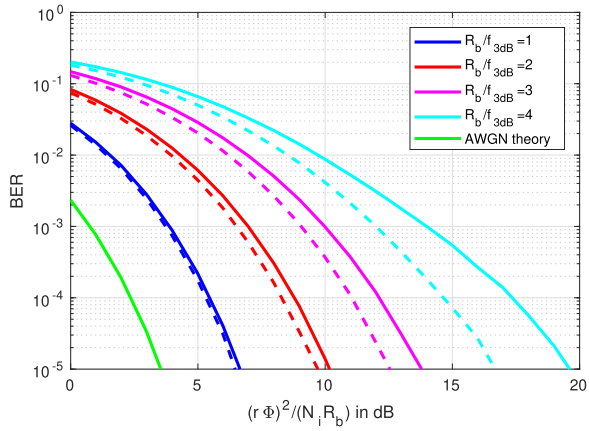

Fig. 15. BER simulations for ACO-HCM-8/2-PAM in the dispersive OWC channel: FEM channel (solid lines) and exponential model (dashed). The corresponding theoretical ACO-HCM curve for the non-dispersive (AWGN) channel is drawn as a reference.

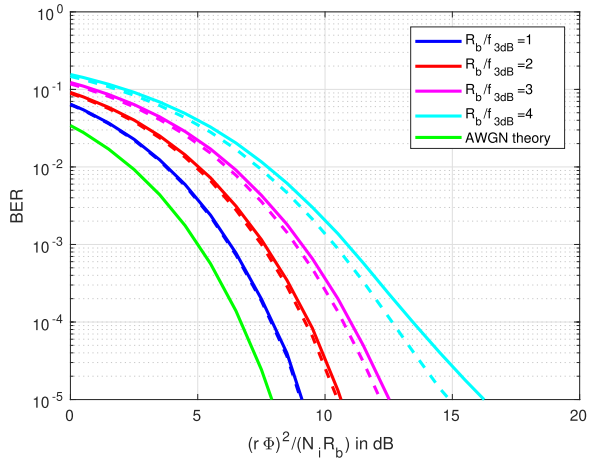

Fig. 16. BER simulations for ACO-HCM-8/4-PAM in the dispersive OWC channel: FEM channel (solid lines) and exponential model (dashed). The corresponding theoretical ACO-HCM curve for the non-dispersive (AWGN) channel is drawn as a reference.

observe a poorer performance for the rate $R_\mathrm{b} = f_{3\,\mathrm{dB}}$ due to the reduced Euclidean distance of the signal constellation and a similar performance for $R_\mathrm{b} = 2f_{3\,\mathrm{dB}}$ compared to OOK-NRZ without equalization. But already for $R_\mathrm{b} = 3f_{3\,\mathrm{dB}}$, the reduced bandwidth corresponding to 48 instead of 96 sub-carriers leads to a significant improvement. Overall, the trade-off between the available SNR $(r\Phi)^2/(N_\mathrm{i}R_\mathrm{b})$ and the achievable bit rate R_b is clearly visible, both for ACO-OFDM and OOK-NRZ. We conclude that for ACO-OFDM is important to choose the optimal modulation level M depending on the channel characteristics. One may also use different modulation levels for different sub-carriers [30] or even apply water-filling techniques [26], [31], which would require knowledge of the channel at the transmitter. Yet, OOK-NRZ in conjunction with ZFE or MLSE equalization at the receiver can be considered a viable alternative. Finally, we note that the exponential model for the diffuse channel components is relatively accurate for low $R_\mathrm{b}/f_{3\,\mathrm{dB}}$ ratios, but rather inaccurate for high $R_\mathrm{b}/f_{3\,\mathrm{dB}}$ ratios, as already observed for OOK-NRZ.

C. BER Simulations for ACO-HCM

As a third example, we consider ACO-HCM [32]. For ACO-HCM-N/M-PAM, a vector of length $N/2$ with M-ary pulse amplitude modulation (PAM) symbols is mapped on a vector of N chips by means of a partial Hadamard transform. Only the Hadamard vectors of odd symmetry are modulated for which the information symbols can be recovered from the clipped signal. ACO-HCM follows similar ideas as ACO-OFDM with the difference that the discrete Fourier transform is replaced by a Hadamard transform, which leads to a Tx signal with a finite set of values. This is beneficial for non-linear transmitters. The values for κ are similar to those for ACO-OFDM, but MLSE reception is only applicable for ACO-HCM and leads to a performance gain. For a dispersive OWC channel, an empty guard chip is added to absorb the ISI. The MLSE receiver then works with the signal vectors including this guard chip and the channel dispersion.We note that the guard chip leads to an increase of κ by the factor $(N+1)/N$.

For the following simulations with the diffuse Barry A channel, $N = 8$ and 2-PAM has been chosen. In Fig. 15, the results are shown for $R_\mathrm{b}/f_{3\,\mathrm{dB}} = 1, 2, 3, 4$. We observe a very good performance for the lower bit rates but a significant degradation as the bit rate increases. This results from the channel attenuation as discussed above. It should be noted that with ACO-HCM, 4 bits are mapped to 8 chips, resulting in a doubling of bandwidth compared to OOK-NRZ. In addition, the guard chip leads to a further increase by the factor 9/8. For the same reasons as discussed above for ACO-OFDM, one should thus take higher-level modulation schemes into account. In Fig. 16, simulations are shown for 4-PAM, which occupies only half the bandwidth compared to 2-PAM at the same bit rate. We observe a significant improvement for $R_\mathrm{b} = 3f_{3\,\mathrm{dB}}$ and $R_\mathrm{b} = 4f_{3\,\mathrm{dB}}$ and a degradation for $R_\mathrm{b} = f_{3\,\mathrm{dB}}$. This corresponds to the aforementioned trade-off between the Euclidean distance of the signal constellation and the channel attenuation.

D. Discussion of the Simulation Results

Comparing the simulation results presented above, we note that it is not possible to make a simple decision about the optimal transmission scheme. OOK-NRZ, which is the simplest optical modulation scheme, performs surprisingly good in the dispersive OWC channel if MLSE is applied. This setup shows the highest robustness in the sense that the dependence on the ratio $R_\mathsf{b}/f_{3\,\mathsf{dB}}$ between bit rate and channel bandwidth is most favorable. Moreover, we found that the degradation can approximately be well described by the electrical gain factor Γ defined in (37). As shown in Fig. 10, even the very simple ZFE leads to acceptable results for OOK-NRZ for all channel parameters considered in our simulations.

ACO-OFDM and ACO-HCM perform better than OOK-NRZ for low $R_\mathsf{b}/f_{3\,\mathsf{dB}}$ ratios, but they are more sensitive at larger $R_\mathsf{b}/f_{3\,\mathsf{dB}}$ ratios. Comparing ACO-OFDM and ACO-HCM we find an advantage for the latter one. This is due to the possibility to apply MLSE, but the cost is of course a higher receiver complexity.

Finally, we found that the exponential model for the diffuse channel components is relatively accurate for low $R_\mathsf{b}/f_{3\,\mathsf{dB}}$ ratios, but tends to be inaccurate for high $R_\mathsf{b}/f_{3\,\mathsf{dB}}$ ratios. This highlights the importance of accurate modeling of the OWC channel, in order to arrive at realistic BER predictions for a wide range of parameters of the employed optical modulation scheme.

VI. Conclusion

We devised a comprehensive modeling procedure for dispersive optical wireless indoor channels in VLC applications – starting from a highly accurate frequency-domain channel emulation method, which was finally linked to precise BER predictions for optical modulation schemes. The advantage of our approach is its generality and wide applicability, as in principle realistic BER predictions can be obtained for arbitrary rooms, customized positions of luminaires and optical receivers, and basically all practically relevant optical modulations schemes. Furthermore, our modeling procedure can readily be extended to an end-to-end electrical channel model as well as to MIMO setups. To considerably improve simulation time, a chip-rate model has been presented based on the Forney formalism, which is well-known from digital radio-transmission systems. We have discussed in detail that optical channel impulse responses should be normalized with respect to the 1-norm instead of the 2-norm and devised a corresponding definition of the SNR, in order to arrive at meaningful BER predictions. Furthermore, we have shown that the dispersive nature of the optical channel impulse response translates into an electrical gain factor $\Gamma < 1$, which can be linked to a corresponding performance loss compared to a (non-dispersive) AWGN channel.

Finally, our modeling procedure was exemplified for OOK-NRZ, ACO-OFDM, and ACO-HCM modulation schemes, which facilitated a rigorous comparison within a common consistent framework. A specific result was that OOK-NRZ with ZFE or MLSE equalization at the receiver offers a quite robust performance, even if the bit rate exceeds the 3-dB bandwidth of the optical channel. ACO-OFDM and ACO-HCM tend to perform better than OOK-NRZ for lower bit rates, but tend to be more sensitive for larger bit rates, while we pointed out some advantages of ACO-HCM over ACO-OFDM. Furthermore, for the examples considered in this paper the widely-employed exponential model for the diffuse channel components proved relatively accurate for low bit rates, but tended to be inaccurate for higher bit rates, which corroborates the importance of accurate modeling of the optical wireless channel.

Appendix

A. End-to-End Electrical Channel Model

In the following, we derive an end-to-end system model for IM/DD OWC systems. The end-to-end system model is depicted in Fig. 2. In the electrical domain, the transmitted bit sequence $\mathbf{b}$ is first modulated onto an analog transmit signal $x_{\mathsf{Tx}}(t)$, which is passed to a driver circuit. The corresponding output current $i_{\mathsf{F}}(t)$ feeds the LED, which emits the optical signal $\phi_{\mathsf{Tx}}(t)$. If the LED is operated in the linear regime, it can be modeled by a frequency response $C_{\mathsf{LED}}(f)$, such that the optical transmit signal may be written as

$$\phi_{\mathsf{Tx}}(t) = \alpha \cdot c_{\mathsf{LED}}(t) * x_{\mathsf{Tx}}(t), \tag{61}$$

where α denotes the proportionality factor associated with the electrical-to-optical conversion (El/O). Note that for single-carrier modulation schemes, such as OOK or PPM, control of signal dynamics is relatively straightforward, whereas for multi-carrier modulation schemes, such as ACO-OFDM, non-linear pre-distortion techniques may be required at the transmitter side [2, Ch. 3], in order to ensure that the linearity assumption is valid.

In the optical domain, the emitted optical signal propagates through the OWC channel and is captured by the PD at the receiver – typically a positive-intrinsic-negative (PIN) PD. The PD converts the received optical signal $\phi_{\mathsf{Rx}}(t)$ back to the electrical domain and yields a corresponding output current $i_{\mathsf{PD}}(t)$. A transimpedance amplifier (TIA) finally delivers the received signal $x_{\mathsf{Rx}}(t)$, which is demodulated to obtain the estimated bit sequence $\hat{\mathbf{b}}$. If the PD is operated in the linear regime and the dynamic range of the TIA is sufficiently large (with the operating point of the PD output current being adjusted accordingly), the PD can be modeled by a frequency response $C_{\mathsf{PD}}(f)$, such that the electrical receive signal may be written as

$$x_{\mathsf{Rx}}(t) = r \cdot c_{\mathsf{PD}}(t) * \phi_{\mathsf{Rx}}(t). \tag{62}$$

Thus, if transmitter and receiver are both operated in the linear regime, we arrive at an all-electrical end-to-end channel model, which includes the *optical* channel impulse response $c(t)$ as a core component:

$$x_{\mathsf{Rx}}(t) = c_{\mathsf{el,ov}}(t) * x_{\mathsf{Tx}}(t), \tag{63}$$

where

$$c_{\mathsf{el,ov}}(t) = r \cdot \eta \cdot \alpha \cdot c_{\mathsf{LED}}(t) * c(t) * c_{\mathsf{PD}}(t). \tag{64}$$

This enables realistic BER predictions for all practically relevant optical modulation schemes, as explained in Section II-C.

REFERENCES

[1] P. A. Hoeher, *Visible Light Communications: Theoretical and Practical Foundations*. Munich, Germany: Carl Hanser, 2019.

[2] S. Dimitrov and H. Haas, *Principles of LED Light Communications: Towards Networked Li-Fi*. Cambridge, U.K.: Cambridge Univ. Press, 2015.

[3] J. Mietzner et al., "Joint light planning and error-rate prediction for dual-use lighting/visible light communication," *IEEE Photon. J.*, vol. 14, no. 6, Dec. 2022, Art. no. 7362113.

[4] K. Lee, H. Park, and J. R. Barry, "Indoor channel characteristics for visible light communications," *IEEE Commun. Lett.*, vol. 15, no. 2, pp. 217–219, Feb. 2011.

[5] S. P. Rodríguez, R. P. Jiménez, B. R. Mendoza, F. J. L. Hernández, and A. J. A. Alfonso, "Simulation of impulse response for indoor visible light communications using 3D CAD models," *EURASIP J. Wireless Commun. Netw.*, vol. 2013, pp. 1–10, Feb. 2013.

[6] A. Tsiatmas, C. P. M. J. Baggen, F. M. J. Willems, J.-P. M. G. Linnartz, and J. W. M. Bergmans, "An illumination perspective on visible light communications," *IEEE Commun. Mag.*, vol. 52, no. 7, pp. 64–71, Jul. 2014.

[7] F. Miramirkhani and M. Uysal, "Channel modeling and characterization for visible light communications," *IEEE Photon. J.*, vol. 7, no. 6, Dec. 2015, Art. no. 7905616.

[8] H. Schulze, "Frequency-domain simulation of the indoor wireless optical communication channel," *IEEE Trans. Commun.*, vol. 64, no. 6, pp. 2551–2562, Jun. 2016.

[9] M. Uysal, F. Miramirkhani, O. Narmanlioglu, T. Baykas, and E. Panayirci, "IEEE 802.15.7R1 reference channel models for visible light communications," *IEEE Commun. Mag.*, vol. 52, no. 1, pp. 212–217, Jan. 2017.

[10] L. Hua, Y. Zhuang, L. Qi, J. Yang, and L. Shi, "Noise analysis and modeling in visible light communication using Allan variance," *IEEE Access*, vol. 6, pp. 74320–74327, 2018.

[11] H. Schulze, "FEM simulations for the wireless optical indoor communication channel," *IET Optoelectron.*, vol. 12, no. 2, pp. 94–105, 2018.

[12] M. Wolf, L. Grobe, M. R. Rieche, A. Koher, and J. Vučić, "Block transmission with linear frequency domain equalization for dispersive optical channels with direct detection," in *Proc. 12th Int. Conf. Transp. Opt. Netw.*, 2010, pp. 1–8.

[13] R. Raj, S. Jaiswal, and A. Dixit, "On the effect of multipath reflections in indoor visible light communication links," *IEEE Access*, vol. 8, pp. 190620–190636, 2020.

[14] J. M. Kahn and J. R. Barry, "Wireless infrared communications," *Proc. IEEE*, vol. 85, no. 2, pp. 265–298, Feb. 1997.

[15] C. A. Bouroussis, D. T. Nikolaou, and F. V. Topalis, "Test report on the validation of Relux Desktop 2019 against CIE 171:2006," May 2019. Accessed: Jan. 25, 2024. [Online]. Available: https://relux.com/assets/static/global/documents/ReluxDesktop_validation_report_Final.pdf

[16] H. Schulze and P. A. Hoeher, "On the general error event probability evaluation of optical intensity modulation schemes," *IEEE Photon. J.*, vol. 14, no. 5, Oct. 2022, Art. no. 7954008.

[17] A. Tsiatmas, F. M. J. Willems, and C. P. M. J. Baggen, "Square root approximation to the poisson channel," in *Proc. IEEE Int. Symp. Inf. Theory*, 2013, pp. 1695–1699.

[18] T. Komine and M. Nakagawa, "Fundamental analysis for visible-light communication system using LED lights," *IEEE Trans. Consum. Electron.*, vol. 50, no. 1, pp. 100–107, Feb. 2004.

[19] J. B. Carruthers and J. M. Kahn, "Modeling of nondirected wireless infrared channels," *IEEE Trans. Commun.*, vol. 45, no. 10, pp. 1260–1268, Oct. 1997.

[20] C. M. Goral, K. E. Torrance, D. P. Greenberg, and B. Battaile, "Modeling the interaction of light between diffuse surfaces," *ACM Comput. Graph.*, vol. 18, no. 3, pp. 213–222, 1984.

[21] M. F. Cohen and J. R. Wallace, *Radiosity and Realistic Image Synthesis*. San Mateo, CA, USA: Morgan Kaufmann, 1993.

[22] J. R. Howell, M. P. Mengüç, and R. Siegel, *Thermal Radiation Heat Transfer*, 7th ed. Boca Raton, FL, USA: CRC Press, 2021.

[23] J. R. Howell, "A catalog of radiation heat transfer configuration factors," 2023. Accessed: Jan. 25, 2024. [Online]. Available: http://www.thermalradiation.net/indexCat.html

[24] J. R. Barry, *Wireless Infrared Communications*. Norwell, MA, USA: Kluwer, 1994.

[25] V. Jungnickel, V. Pohl, S. Nönnig, and C. von Helmolt, "A physical model of the wireless infrared communication channel," *IEEE J. Sel. Areas Commun.*, vol. 20, no. 3, pp. 631–640, Apr. 2002.

[26] X. Li, J. Vucic, V. Jungnickel, and J. Armstrong, "On the capacity of intensity-modulated direct-detection systems and the information rate of ACO-OFDM for indoor optical wireless applications," *IEEE Trans. Commun.*, vol. 60, no. 3, pp. 799–809, Mar. 2012.

[27] G. D. Forney, "Maximum-likelihood sequence estimation of digital sequences in the presence of intersymbol interference," *IEEE Trans. Inf. Theory*, vol. 18, no. 3, pp. 363–378, May 1972.

[28] J. Proakis and M. Salehi, *Digital Communications*, 5th ed. New York, NY, USA: McGraw-Hill, 2008.

[29] J. Armstrong, B. J. Schmidt, D. Kalra, H. A. Suraweera, and A. J. Lowery, "Performance of asymmetrically clipped optical OFDM in AWGN for an intensity modulated direct detection system," in *Proc. IEEE Glob. Commun. Conf.*, 2006, pp. 1–5.

[30] S. K. Wilson and J. Armstrong, "Transmitter and receiver methods for improving asymmetrically-clipped optical OFDM," *IEEE Trans. Wireless Commun.*, vol. 8, no. 9, pp. 4561–4567, Sep. 2009.

[31] S. Mazahir, A. Chaaban, H. Elgala, and M.-S. Alouini, "Achievable rates of multi-carrier modulation schemes for bandlimited IM/DD systems," *IEEE Trans. Wireless Commun.*, vol. 18, no. 3, pp. 1957–1973, Mar. 2019.

[32] H. Schulze and P. A. Hoeher, "Asymmetrically clipped optical Hadamard coded modulation (ACO-HCM)," *IEEE Photon. J.*, vol. 15, no. 1, Feb. 2023, Art. no. 7300512.